C. R. Mecanique 346 (2018) 770–778

Contents lists available at ScienceDirect

Comptes Rendus Mecanique

www.sciencedirect.com

Computational modeling of material forming processes / Simulation numérique des procédés de mise en forme

Modelling of the blanking process of high-carbon steel using Lemaitre damage model

Kerim Isik [a,*], Yoshinori Yoshida [b], Lin Chen [c], Till Clausmeyer [a], A. Erman Tekkaya [a]

[a] Institute of Forming Technology and Lightweight Components, TU Dortmund University, Baroper Str. 303, 44227 Dortmund, Germany
[b] Center for Advanced Die Engineering and Technology (G-CADET), Gifu University, 1-1 Yanagido, 501-1193 Gifu, Japan
[c] CW Bearing GmbH, Am Neumarkt 34/36, 22041 Hamburg, Germany

ARTICLE INFO

Article history:
Received 29 August 2017
Accepted 9 April 2018
Available online 25 June 2018

Keywords:
Damage model
Parameter identification
Blanking
Shear fracture

ABSTRACT

This paper presents a methodology to model a blanking process using a continuum mechanical damage model. A variant of the Lemaitre model, in which the quasi-unilateral conditions are taken into consideration to modify the damage behavior under compressive stress states, is selected as material model. S45C high-carbon steel is analyzed experimentally. To characterize the damage behavior of the material, notched round bar tensile tests with three different notch radii (6 mm, 10 mm, and 20 mm) using image analysis are performed. Using digital image processing, the strain at the deformation zone can be computed for the load–strain curves. Those curves are used as an objective function to determine the parameters of the Lemaitre damage model. The experimental results are compared with the results of the FE analysis of the tensile test. The identified model parameters are used in numerical investigations of axisymmetric blanking. The effect of the model's extension to quasi-unilateral damage evolution is discussed. The crack progress in high-carbon steel sheet during blanking and the final sheared part morphology are predicted and compared with the experimental results. Sheared surface and burr height obtained by the analysis coincide with the results of the blanking experiment.

1. Introduction

Shear-cutting processes require separation of the material from the remaining workpiece. There are various shear-cutting operations such as blanking, trimming, guillotining, punching, and adiabatic shearing, each of which has a certain experimental setup and a set of process parameters. Plastic flow, fracture behavior (material properties) and friction (process parameters) influence the resulting fracture's surface properties [1]. To minimize the efforts for the process design, the predictions of surface quality and required maximum force by cutting machine are mandatory. Especially for sheet metal cutting operations, there are several analytical models to predict the required maximal shearing force and the fraction of sheared and fracture surface to assign the sheared surface quality [2,3]. Application of finite element models using damage models ease and improve these predictions. Hambli [4] used the Lemaitre damage model [5] to simulate fine blanking

* Corresponding author.
E-mail addresses: kerim.isik@iul.tu-dortmund.de (K. Isik), yyoshida@gifu-u.ac.jp (Y. Yoshida), chen.15@gmx.de (L. Chen), till.clausmeyer@iul.tu-dortmund.de (T. Clausmeyer), erman.tekkaya@iul.tu-dortmund.de (A. Erman Tekkaya).

https://doi.org/10.1016/j.crme.2018.05.003
1631-0721/

Table 1
Some application examples for Lemaitre model and its variants.

Study	Model specification	Test for characterization	Process
Hambli [4]	Isotropic standard model	Tensile test	Sheet fine blanking
Hambli [7]	Isotropic standard model	Tensile test	Sheet blanking
Gutknecht et al. [10]	Crack-closure enhancement	Notched tensile test In-plane shear test	Sheet blanking
Bouchard et al. [11]	Crack-closure enhancement	Notched tensile test	Cold forging, extrusion

(1% clearance) and showed that the Lemaitre Model is incapable to model the fine blanking process of 4-mm-thick sheets. Hambli [4] suggested that the application of Rice and Tracey's model [6] provides better prediction for crack initiation and propagation. On the contrary, Hambli [7] showed that the Lemaitre model provides better prediction for the blanking process (10% clearance), compared to the Gurson Model [8] for a relatively thick sheet (3.5 mm in sheet thickness). In this study, the predictive capability of a variant of the Lemaitre model is investigated with a moderately thick workpiece (thickness of 1.2 mm). In further studies, the Lemaitre model and its variants are used to model the onset of fracture (Table 1). The most common enhancement of the Lemaitre model is related to the effect of the compressive stress states, crack-closure phenomenon presented in [9]. For the cutting process, especially the studies are concentrating on the sheet metals (as in the studies of Hambli [4] and [7] and Gutknecht et al. [10]). Bouchard et al. investigated the application of the Lemaitre model with crack-closure for more classic bulk forming operations such as cold forging and extrusion [11]. In this work, blanking of a bulk material is investigated. The specimens are cut from bulk material.

In general, material anisotropy is more critical for sheet materials than for bulk ones, because of texture due to the preforming procedure (rolling, etc.). The cutting operations take place in the through-thickness direction, which is not directly related to the planar anisotropy of the sheet. From this point of view, the cutting operation is not a typical sheet forming operation, during which in-plane plane-stress conditions are dominant.

In this paper, the blanking process for a bulk material is modeled using a variant of the Lemaitre model, which is extended to unilateral damage evolution to distinguish damage accumulation for tensile and compressive stress states [9]. The details of this damage model are presented in Section 2. The experimental procedures for material characterization and blanking experiments are explained in Section 3. Section 4 includes the details of finite element simulations of the characterization and blanking tests. The simulation results and comparisons with experiments are discussed in Section 5 and, finally, conclusions are drawn in Section 6.

2. Lemaitre model with a quasi-unilateral damage evolution

2.1. General framework

In the Lemaitre model family, the material deterioration is measured by the damage variable D. More specifically, D stands for the phenomenological construct, which is a measure for homogenized microvoids and microcracks in the material. The limits are $D = 0$ for undamaged material and $D = D_{\text{critical}}$ for the complete material deterioration.

The Lemaitre model according to [12] belongs to the class of thermo-dynamically consistent models. Here thermo-dynamically consistency means that the dissipation

$$0 \leq \Omega = \mathbf{T} : \dot{\mathbf{E}} - \dot{\Psi} \tag{1}$$

is always non-negative. $\mathbf{T}$ is an arbitrary stress tensor and $\mathbf{E}$ the thermo-dynamically conjugate strain tensor. In (1), "$:$" denotes the double contraction product.

$$\Psi = \Psi(\boldsymbol{\chi}) \quad \text{with } \boldsymbol{\chi} = \left\{\mathbf{E}^{\mathrm{e}}, \alpha, D, T_{\text{temp}}\right\}^{\intercal} \tag{2}$$

represents the Helmholtz free energy, a positive and convex function with respect to its argument $\boldsymbol{\chi}$. The superscript "$\intercal$" denotes the transpose of a vector or tensor. In the case of the Lemaitre model, common choices for $\boldsymbol{\chi}$ are $\mathbf{E}^{\mathrm{e}}$ for the elastic part of the strain tensor, D for the scalar damage variable, α for the scalar isotropic hardening variable, and T_{temp} for the temperature. Here, the fact that the plastic part $\mathbf{E}^{\mathrm{p}}$ of the total strain $\mathbf{E}$ does not modify the stored or reversible energy is exploited. One obtains $\mathbf{T} = \partial_{\mathbf{E}^{\mathrm{e}}} \Psi$ from (1), where $\partial_{\circ}(\bullet)$ denotes $\partial(\bullet)/\partial_{\circ}$. Similar stress-like driving forces q and Y are given by

$$\begin{aligned} q &= \partial_{\alpha} \Psi(\mathbf{E}^{\mathrm{e}}, \alpha, D, T_{\text{temp}}) \\ Y &= -\partial_{D} \Psi(\mathbf{E}^{\mathrm{e}}, \alpha, D, T_{\text{temp}}) \\ s &= \partial_{T_{\text{temp}}} \Psi(\mathbf{E}^{\mathrm{e}}, \alpha, D, T_{\text{temp}}) \end{aligned} \tag{3}$$

for the isotropic hardening and the damage, respectively. s denotes the specific entropy.

Substitution of the state equations (3) back in (1) yields the mechanical portion of the reduced dissipation inequality Ω^m for purely mechanical conditions without temperature effects:

$$0 \leq \Omega^m = \mathbf{T} : \dot{\mathbf{E}}^{\mathrm{p}} - q\dot{\alpha} + Y\dot{D} \tag{4}$$

2.2. Special model choices

The model formulation requires the selection of a kinematic framework which governs the elastoplastic material behavior. In the current model, the multiplicative split of the total deformation gradient, which has an elastic $\mathbf{F}^{\mathrm{e}}$ and plastic part $\mathbf{F}^{\mathrm{p}}$ as proposed by Lee [13], is:

$$\mathbf{F} = \mathbf{F}^{\mathrm{e}} \cdot \mathbf{F}^{\mathrm{p}} \tag{5}$$

The kinematic formulation of the model relies on an approximation for the logarithmic, elastic stretch $\mathbf{U}^{\mathrm{e}}$, which arises in the context of the polar decomposition $\mathbf{F}^{\mathrm{e}} = \mathbf{R}^{\mathrm{e}} \cdot \mathbf{U}^{\mathrm{e}}$, with $\mathbf{R}^{\mathrm{e}}$ the elastic rotation tensor. As demonstrated in [14]:

$$\frac{\mathrm{d}}{\mathrm{d}t} \ln\left(\mathbf{U}^{\mathrm{e}}\right) = \mathbf{R}^{\mathrm{e}} \cdot \mathbf{D} \cdot \mathbf{R}^{\mathrm{e}\intercal} - \mathbf{D}^{\mathrm{p}} \tag{6}$$

$$\dot{\mathbf{R}}^{\mathrm{e}} = \mathbf{W} \cdot \mathbf{R}^{\mathrm{e}} - \mathbf{R}^{\mathrm{e}}\mathbf{W}^{\mathrm{p}} \tag{7}$$

for small elastic strain, i.e. $\left|\ln\left(\mathbf{U}^{\mathrm{e}}\right)\right| \ll 1$. The rate of total deformation $\mathbf{D} = \mathrm{sym}\,(\mathbf{L})$ is given in terms of the "velocity gradient" $\mathbf{L} = \dot{\mathbf{F}}^{\mathrm{p}} \cdot \mathbf{F}^{-1}$. Consequently, $\mathbf{D}^{\mathrm{p}} = \mathrm{sym}\left(\mathbf{L}^{\mathrm{p}}\right) = \mathrm{sym}(\dot{\mathbf{F}}^{\mathrm{p}} \cdot \dot{\mathbf{F}}^{-1})$ and $\mathbf{W}^{\mathrm{p}} = \mathrm{skw}(\mathbf{L}^{\mathrm{p}})$ represent the rate of plastic rotation and the plastic spin, respectively. The assumption $\mathbf{W}^{\mathrm{p}} \approx \mathbf{0}$ is justified for the investigated metals, so that the axes of the material rotate with the continuum, and consequently $\mathbf{R}^{\mathrm{e}} = \mathbf{R}$, with $\mathbf{R}$ the rigid body rotation.

In light of Eqs. (5)–(7), the model is formulated in terms of the back-rotated Cauchy stress:

$$\mathbf{M} = \mathbf{R}^{\mathrm{e}\intercal} \cdot \mathbf{T} \cdot \mathbf{R}^{\mathrm{e}} \tag{8}$$

The evolution relations

$$\begin{aligned} \mathbf{D}^{\mathrm{p}} &= \lambda \partial_{\mathbf{M}} \Phi(\mathbf{M}, q, Y; D) \\ \dot{\alpha} &= -\lambda \partial_q \Phi(\mathbf{M}, q, Y; D) \\ \dot{D} &= \lambda \partial_Y \Phi(\mathbf{M}, q, Y; D) \end{aligned} \tag{9}$$

for $\mathbf{D}^{\mathrm{p}}$, $\dot{\alpha}$ and $\dot{D}$ making use of the generalized normality rule require the choice of a specific dissipation potential. It is split into a plastic Φ^{p} and a damage part Φ^{D}:

$$\Phi = \Phi^{\mathrm{p}}(\mathbf{M}, q, D) + \Phi^{\mathrm{D}}(Y, D) \tag{10}$$

Φ^{p} distinguishes between an elastic domain $\Phi^{\mathrm{p}} \leq 0$ and an anisotropic plastic domain.

A Hill-type form according to [15]

$$\Phi^{\mathrm{p}}(\mathbf{M}, q, D) = \tilde{\sigma}_{\mathrm{eq}} - q \tag{11}$$

is chosen, where $\tilde{\sigma}_{\mathrm{eq}} = \sqrt{\tilde{\mathbf{M}} : \mathbf{H} : \tilde{\mathbf{M}}}$ represents the effective equivalent stress with the fourth-order tensor $\mathbf{H}$ accounting for the texture of the material. $\tilde{\mathbf{M}} = \mathbf{M}/(1 - D)$ is the effective stress considering the effect of damage. The damage potential [16]:

$$\Phi^{\mathrm{D}} = \frac{S}{(\delta + 1)} \left\langle \frac{Y - Y_0}{S} \right\rangle^{\delta+1} \frac{1}{(1 - D)^{\beta}} \tag{12}$$

introduces a threshold for damage initiation by means of the Macaulay brackets $\langle \bullet \rangle = \left\{ \begin{smallmatrix} 0 \text{ for } \bullet < 0 \\ \bullet \text{ for } \bullet \geq 0 \end{smallmatrix} \right\}$ β, S, Y_0 and δ are material parameters governing the evolution of damage.

For the model variant that weighs the effect of compressive stress states by introducing an additional scaling parameter (crack-closure parameter) h, the modified elastic energy density expression becomes [9]:

$$Y = \frac{1 + \nu}{2E} \left[\frac{\langle M_{ij} \rangle \langle M_{ij} \rangle}{(1 - D)^2} + h \frac{\langle -M_{ij} \rangle \langle -M_{ij} \rangle}{(1 - hD)^2} \right] - \frac{\nu}{2E} \left[\frac{\langle M_{kk} \rangle^2}{(1 - D)^2} + h \frac{\langle -M_{kk} \rangle^2}{(1 - hD)^2} \right] \tag{13}$$

where ν is Poisson's ratio and E is Young's modulus.

For $h = 0$, only tensile stresses are effective in the damage evolution, whereas for $h = 1$ the model boils down to the original Lemaitre model. For a value of h between zero and one, $0 < h < 1$, just a part of the compression stresses will be considered for the evolution of damage.

Table 2
Mechanical properties of the material S45C.

Young's modulus E [GPa]	Poisson's ratio ν	Yield strength σ_0 [MPa]	Hardening law	
			C [MPa]	n
199.15	0.29	414	1210	0.217

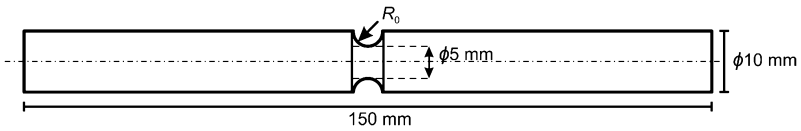

Fig. 1. Dimension of the tensile test specimens (circumferential notched round bar).

With the given framework the following evolutionary equations can be derived,

$$\begin{aligned} \mathbf{D}^{\mathrm{p}} &= \lambda \frac{1}{(1-D)\,\tilde{\sigma}_{\mathrm{eq}}} \mathbf{H} : \left(\tilde{\mathbf{M}}\right) \\ \dot{\alpha} &= \lambda \\ \dot{D} &= \lambda \left\langle \frac{Y - Y_0}{S} \right\rangle^{\delta} \frac{1}{(1-D)^{\beta}} \end{aligned} \tag{14}$$

which completes the material model derivations. The stress update is given by the isotropic form

$$\dot{\mathbf{M}} = (1-D)\left(\mu_1 \operatorname{tr}\left(\mathbf{R}^{\mathrm{e}} \cdot \mathbf{D} \cdot \mathbf{R}^{\mathrm{e}\intercal} - \mathbf{D}^{\mathrm{p}}\right)\mathbf{1} + 2\mu_2\left(\mathbf{R}^{\mathrm{e}} \cdot \mathbf{D} \cdot \mathbf{R}^{\mathrm{e}\intercal} - \mathbf{D}^{\mathrm{p}}\right)\right) \tag{15}$$

where μ_1 and μ_2 denote Lamé's first and second parameters, respectively, which can be represented in terms of the Poisson ratio, ν, and the elasticity modulus, E:

$$\begin{aligned} \mu_1 &= \frac{E\nu}{(1+\nu)(1-2\nu)} \\ \mu_2 &= \frac{E}{2(1+\nu)} \end{aligned} \tag{16}$$

The material model is implemented via the VUMAT interface into the commercial finite-element code ABAQUS [17].

3. Experimental methods

The deformation behavior of S45C high-carbon steel is modeled with the isotropic hardening law with isotropic damage evolution. The elastic material parameters are Young's modulus, E, and Poisson's ratio, ν. Plastic flow curve expression (hardening law) with $\sigma_y(\alpha) = C\alpha^n$, where C and n are material parameters, is used. Those elastoplastic material parameters are listed in Table 2.

3.1. Circumferential notched round bar tensile test using image analysis

In order to characterize the material for the damage model, tensile tests with three different notch geometries are performed. The specimens have the initial notched radii, R of 6, 10, and 20 mm, which have different stress states in the deformation zone (Fig. 1). The load and strain curves obtained from the tests are used in the inverse parameter identification algorithm. To measure the load–strain response of the experiments, image analysis is coupled with the force measurement of the universal testing machine.

3.2. Bridgman's stress analysis

Analysis of normal stress components in necking was carried out by Bridgman [18]. The axial and radial stresses σ_z and σ_r are calculated by the following equations,

$$\sigma_z = \sigma_0 \cdot \left\{1 + \ln\left(\frac{a^2 + 2aR + r^2}{2R}\right)\right\} \tag{17}$$

$$\sigma_r = \sigma_\theta = \sigma_0 \cdot \ln\left(\frac{a^2 + 2aR + r^2}{2R}\right) \tag{18}$$

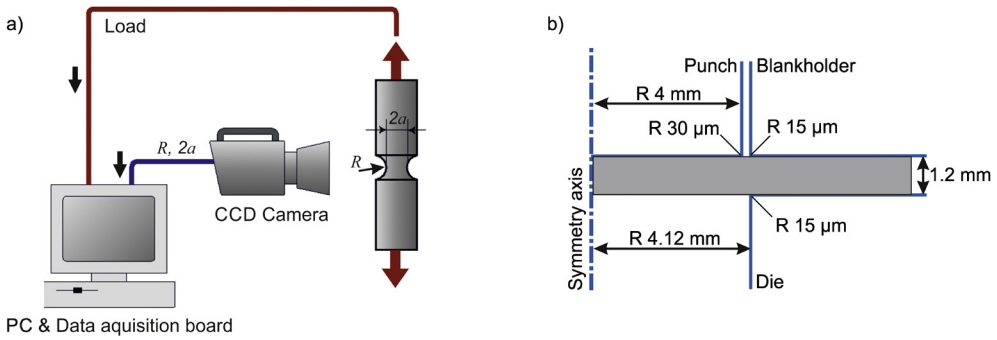

Fig. 2. a) Schematic diagram of the tension test system using image analysis [19], b) sketch of the experimental setup for blanking.

where σ_0 is flow stress, a and R are necking radius and necking curvature radius, respectively. r is the distance from longitudinal center axis. σ_z is the maximum principal stress. There is a relation between the average tensile stress σ_{z_ave} and the tensile load,

$$\sigma_0 \left(1 + \frac{2R}{a}\right) \ln\left(1 + \frac{a}{2R}\right) = \frac{load}{\pi a^2} = \sigma_{z\_ave} \tag{19}$$

Thus, if the change in the necking shape (a and R) and load are measured, all stress components are calculated by Eqs. (17) and (18). The equivalent strain at necking is expressed as:

$$\varepsilon_{eq} = 2 \ln \frac{d_0}{d} \tag{20}$$

where d is the diameter at the notch root and d_0 is the initial value of d. Stress triaxiality is calculated by [19] as follows:

$$\frac{\sigma_m}{\overline{\sigma}} = \frac{1}{3} + \ln\left(\frac{a}{2R} + 1\right) \tag{21}$$

3.3. Image analysis

The contour of the deformation zone (notched area) of a test piece is photographed with a CCD camera (Fig. 2a). The image is processed into a monochrome picture to measure a and R during the test. The load measurement is taken from a universal testing machine.

3.4. Axisymmetric blanking process

The experiment of axisymmetric blanking process is carried out at room temperature by using a hydraulic press. The S45C steel part has an initial thickness of 1.2 mm. Fig. 2b shows the experimental blanking conditions. The punch radius of the circular punch is 4.0 mm, and the clearance between punch and die is 0.12 mm (10% of part thickness). The die tip radius and punch tip radius are 0.015 mm and 0.030 mm, respectively. The sheared surface length and burr height of the blanked disk are measured by using a laser microscope. The punch force and displacement are recorded for comparison with the simulations.

4. Finite element analysis of the experiments

4.1. FE analysis of circumferential notched round bar tensile test

In order to acquire the damage parameters in the Lemaitre model, 3D finite element analysis of a round notched bar tensile test using this model is performed. Considering the symmetry of the specimen and loading, only 1/2 of the whole geometry is simulated using the axisymmetrical model. In the finite element model of this test, 4-node bilinear axisymmetric quadrilateral elements are utilized. Because of the mesh dependency of the local damage models, a constant mesh size is used for parameter identification and blanking experiments. The minimum mesh size is taken as 0.01 mm, which is appropriate for the blanking experiments with a clearance of 0.12 mm and die tip radius 0.015 mm. This minimum mesh size is applied at the deformation zone of the specimen, namely at the center of the round notched bar. An inverse calibration method based on the Lemaitre damage model is developed. The inverse parameter optimization algorithm compares the load–strain curves from simulations with experimental results and adjusts the model parameters to minimize the difference between those results. The obtained material parameters are shown in Table 3.

Table 3
Mechanical properties of the S45C material.

S [MPa]	Y_0 [MPa]	β	δ	D_{critical}
6.51	0.30	1.36	1.64	0.21

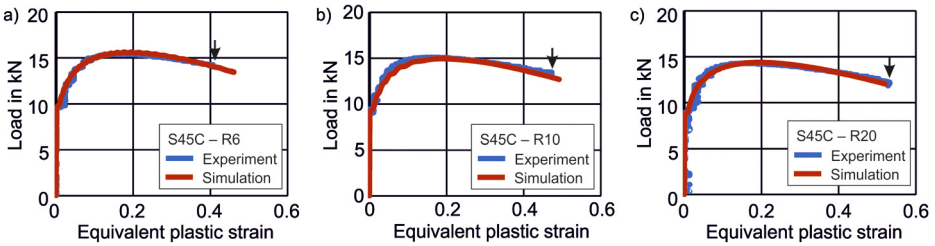

Fig. 3. Load–strain comparison for experiment and simulation at the center of the notched tensile specimens with a notch radius of a) 6 mm, b) 10 mm, and c) 20 mm (the arrows show the fracture point for the experimental curve).

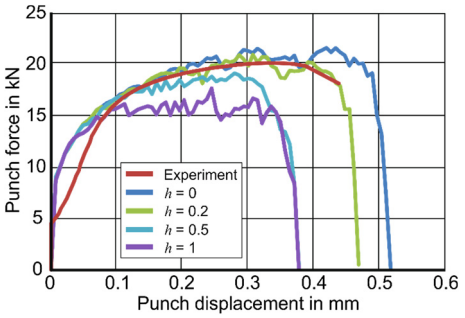

Fig. 4. The effect of h on the punch force–displacement curve.

4.2. FE analysis of axisymmetric blanking

Due to symmetry conditions, the examined blanking process can be simulated as an axisymmetric plane-strain model. The die, blank holder and the punch are modeled as rigid curves, whereas the sheet is modeled as a deformable body. The punch velocity is 35 mm/s as in the experiment. In order to reduce the computational time, the mesh size used for the parameter identification is applied only in the deformation zone. The remaining part is meshed with a coarser mesh. To show the effect of mesh size, a simulation with finer mesh (0.003 mm) and one with coarser mesh (0.02 mm) are compared with the reference one. The cracks are modeled using element deletion technique, such that the elements are removed, as the critical damage value is reached.

5. Results and discussion

5.1. Identification of damage model parameters

The calibration procedure is performed for the experimental tensile load-equivalent plastic strain curve, in which numerical simulations of the notched tensile test are iteratively conducted with a set of damage parameters until the experimental tensile load-equivalent plastic strain curve matches with the calculated curve. The final simulated tensile load-equivalent plastic strain curves obtained are compared with the experimental results (Fig. 3).

The selected specimens are deformed under tension. Consequently, there is no compressive stress component. Therefore, the model parameters, except the crack-closure parameter h, can be identified using those tests. The influence of the crack-closure parameter is discussed using the blanking simulations. The comparison of the experimental and numerical punch force–displacement curves shows that the original Lemaitre model ($h = 1$), underestimates the critical punch displacement for crack initiation. Partial contribution of compressive stress states results in a delayed crack initiation for the material. The simulation with crack-closure parameter $h = 0.2$ matches well with the required maximum force value and the fracture initiation point. This value is similar to the typical values mentioned for metallic materials in [20]. All simulations show a steeper increase compared to the experimental curve during the initial deformation stage. This can be explained by the elastic deformation of the complete punching system. This additional deformation is not considered in the simulations. Thus, the predicted response is stiffer (Fig. 4). For the same reason, the tested penetration distance where the maximum force is achieved is larger in the experiment than in the simulation. The load–displacement curves in Fig. 4 show that the introduc-

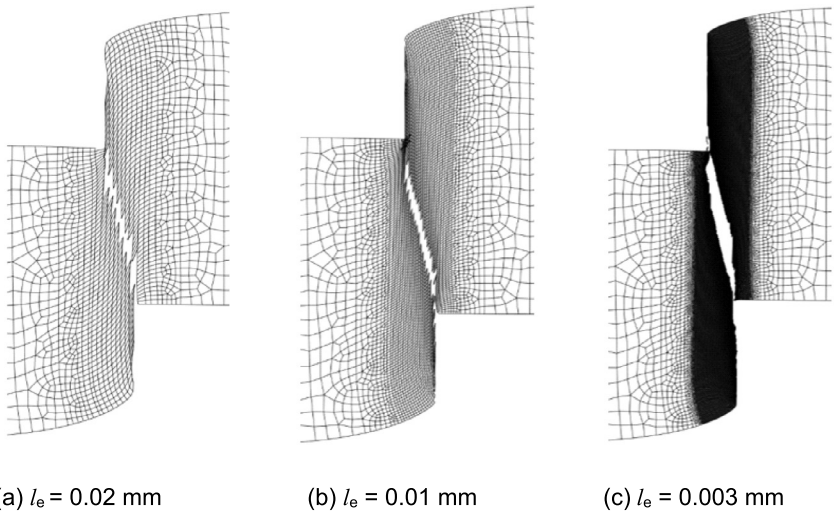

Fig. 5. The effect of minimum element size (l_e) on fracture pattern at a punch displacement of 0.48 mm.

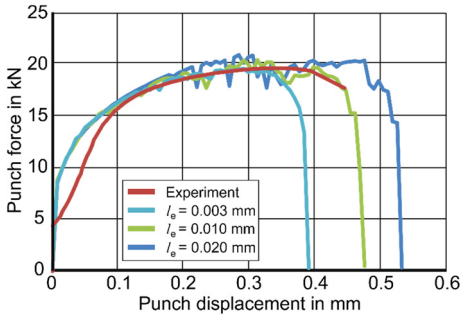

Fig. 6. The effect of mesh size on the force–displacement curves.

tion of the unilateral damage evolution coefficient (h) results in an increase of the peak force as well as a delayed onset of fracture. This behavior is physically reasonable, since with the modified model, compressive stresses delay the evolution of damage.

5.2. Comparison of sheared part morphology

In the blanking process, intensive plastic deformation and damage localize in the area between punch and die. In order to correctly simulate the damage localization and crack path, a mesh size study is conducted by comparing the results of three different mesh sizes in the intensive blanking region. The minimum mesh size of the three mesh patterns are 0.02 mm, 0.01 mm, and 0.003 mm, as shown in Fig. 5, respectively.

The fluctuation near the maximum force of the load curve observed in simulations is caused by the reduction of the structural stiffness due to element deletion during punch translation (Fig. 6). The fluctuation is less serious when the mesh size is smaller, because smaller discontinuities occur when the deleted elements are smaller. Another notable effect of the mesh size on the load–displacement curve is the critical fracture point, where the punch force starts to decrease sharply (Fig. 6).

Based on the experiment and simulation results, the physical mechanisms leading to the complete failure of the sheet material are analyzed as follows: at the first step, the punch and die penetrate the sheet gradually without obvious crack initiation. Damage accumulates intensively in the region between punch and die, until the punch penetrates by 30–35% into the thickness of the specimen.

In this case, because the die tip radius is only half of the punch tip radius, there is a more severe damage effect in the die tip's vicinity, which also leads to earlier crack propagation at the die tip with respect to the punch tip. Then the crack tips propagate quickly to meet each other and create the whole crack path. The damage contours for various simulation steps are depicted in Fig. 7. Damage contours show that the central lines of the maximum damage area are very close to the cutting surface profile. Crack initiation takes place near the contact surface of punch and workpiece.

To assign the sheared and fractured surface ratios at the cutting zone, the experimental sheared edge is examined using a laser microscope. These measurements are compared with the predicted sheared edge using the enhanced Lemaitre damage

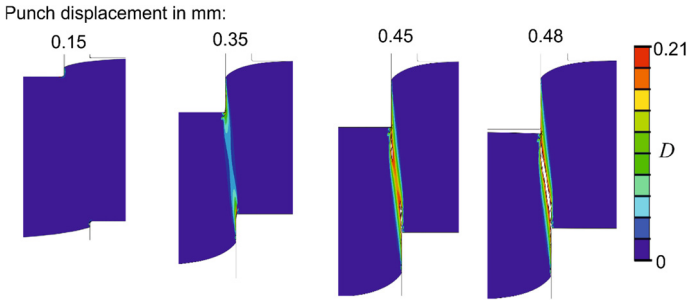

Fig. 7. Damage distributions for the given punch displacements.

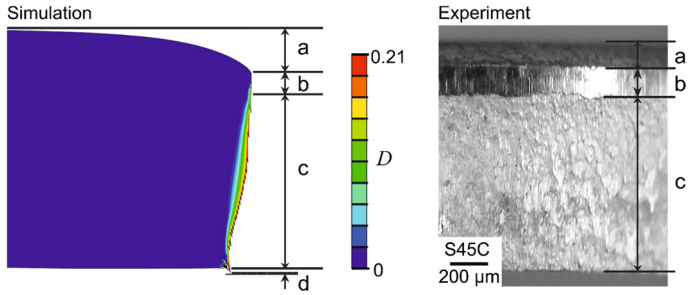

Fig. 8. Experimentally determined and simulated cutting surface from the simulation with the Lemaitre model using the model parameters in Table 3. The measurements are listed in Table 4.

Table 4
Length of the characteristic zones of the cutting surface (shown in Fig. 8) for the experiment, and simulation with various values of the crack-closure parameter, h.

h	a (mm)	b (mm)	c (mm)
0	0.181	0.199	0.820
0.2	0.179	0.244	0.777
0.5	0.166	0.407	0.627
Experiment	0.133	0.143	0.924

model. The quality of the cutting surface is described by the cutting surface parameters. From a typical cutting surface, four characteristic zones can be distinguished (shown in Fig. 8). They are (a) the shear droop area (die-roll width), (b) the burnished area (smooth cut section height), (c) the fractured surface, and (d) the burr.

The comparison of the simulation results with the photographs of the cutting surface reveals that similar distribution of the different cutting areas in the simulation and experiment (Fig. 8 and Table 4). Although the absolute values are different, the tendencies have been accounted for to improve the model ($h = 0$ and $h = 0.2$). For the experiment, the shear drop height and burnished surface length are close to each other (0.133 mm and 0.143 mm). By applying the crack-closure parameter, this relativity can be satisfied better. The overestimation of the shear drop area in simulation could be explained as the springback phenomenon after unloading.

6. Conclusions

Blanking is a shear stress state dominant material removal process, during which a compressive stress state exists. In order to describe material deterioration under shear and compression stress state appropriately, the applied damage model should give distinct predictive performances under tensile, shear, and compressive principal stress states. For this purpose, a variant of the Lemaitre model, extended for unilateral damage evolution to distinguish the damage accumulation for tensile and compressive stress states, is taken into consideration. In this model variant, the crack-closure parameter, h, scales the contribution of the compression stresses for the damage evolution. Lemaitre proposed a value in the range between 0 and 0.2 for metallic materials for this parameter [20]. For the material selected, S45C, the simulation result with $h = 0.2$ matches the experimentally investigated ones on the manner of maximum force and fracture initiation point for blanking experiments. The remaining model parameters are identified by using tensile tests with three different notch radii, at which only tensile stress states are effective. Because of the mesh size dependency of the model, a constant mesh size for the simulations of the characterization and blanking tests is selected. Changing mesh size (0.003 mm, 0.010 mm, and 0.020 mm) alters the predictions for the blanking process excessively. Compared to the blanking simulations, the difference

between the simulations of the notched tests with mesh sizes (0.010 mm and 0.020 mm) is negligible. The identified model parameters are valid for the selected constant mesh size for the parameter identification. The cutting surface comparisons show that application of the model with a crack-closure improves the prediction related to the proportion of the shear droop area (die-roll width) to the burnished area. Hambli [7] showed that the basic Lemaitre model can predict crack initiation during blanking for the investigated sheet in his studies by comparing only the force–displacement curves. However, for the presented material (S45C), the basic Lemaitre model cannot predict crack initiation during blanking. By applying an improvement to the crack-closure model, not only crack initiation but also the cutting surface properties can be predicted appropriately.

Acknowledgements

The authors gratefully acknowledge funding by the German Research Foundation (DFG) within the scope of the Transregional Collaborative Research Centre on sheet-bulk metal forming (SFB/TR 73) in the subproject C4 ‘Analysis of load history dependent evolution of damage and microstructure for the numerical design of sheet-bulk metal forming processes’.

Lin Chen thanks for support by the German Academic Exchange Service (DAAD) through grant 91540220 (Research Grants for Doctoral Candidates).

References

[1] A.G. Atkins, Surfaces produced by guillotining, Philos. Mag. 43A (1981) 627–641.
[2] A.G. Atkins, On cropping and related processes, Int. J. Mech. Sci. 22 (1980) 215–231.
[3] P.A.F. Martins, A.G. Atkins, Revisiting the empirical relation for the maximum shearing force using plasticity and ductile fracture mechanics, J. Mater. Process. Technol. 213 (9) (2013) 1516–1522.
[4] R. Hambli, Finite element simulation of fine blanking processes using a pressure-dependent damage model, J. Mater. Process. Technol. 116 (2–3) (2001) 252–264.
[5] J. Lemaitre, A continuous damage mechanics model for ductile fracture, J. Eng. Mater. Technol. 107 (1985) 83–89.
[6] J.R. Rice, D.M. Tracey, On the ductile enlargement of voids in triaxial stress fields, J. Mech. Phys. Solids 17 (1969) 201–217.
[7] R. Hambli, Comparison between Lemaitre and Gurson damage models in crack growth simulation during blanking process, Int. J. Mech. Sci. 43 (12) (2001) 2769–2790.
[8] V. Tvergaard, A. Needleman, Analysis of cup-cone fracture in a round tensile bar, Acta Metall. 32 (1) (1984) 157–169.
[9] P. Ladevèze, J. Lemaitre, Damage effective stress in quasi-unilateral condition, in: IUTAM Congress, Lyngby, Denmark, 1984.
[10] F. Gutknecht, F. Steinbach, T. Hammer, T. Clausmeyer, W. Volk, A.E. Tekkaya, Analysis of shear cutting of dual phase steel by application of an advanced damage model, Proc. Struct. Integr. 2 (2016) 1700–1707.
[11] P.O. Bouchard, L. Bourgeon, S. Fayolle, K. Mocellin, An enhanced Lemaitre model formulation for materials processing damage computation, Int. J. Mater. Form. 4 (3) (2010) 299–315.
[12] J. Lemaitre, A. Benallal, D. Marquis, Lifetime prediction of structures in anisothermal viscoplasticity coupled to damage, Nucl. Eng. Des. 133 (1992) 345–360.
[13] E.H. Lee, Elastic–plastic deformation at finite strains, J. Appl. Mech. 36 (1) (1969) 1–6.
[14] T. Clausmeyer, B. Svendsen, Comparison of two models for anisotropic hardening and yield surface evolution in bcc sheet steels, Eur. J. Mech. A, Solids 54 (2015) 120–131.
[15] R. Hill, A theory of the yielding and plastic flow of anisotropic metals, Proc. R. Soc. Lond. Ser. A, Math. Phys. Sci. 193 (1033) (1948) 281–297.
[16] K. Saanouni, On the numerical prediction of the ductile fracture in metal forming, Eng. Fract. Mech. 75 (2008) 3545–3559.
[17] C. Soyarslan, A.E. Tekkaya, A damage coupled orthotropic finite plasticity model for sheet metal forming: CDM approach, Comput. Mater. Sci. 48 (1) (2010) 150–165.
[18] P.W. Bridgman, Studies in Large Plastic Flow and Fracture, McGraw-Hill, New York, 1952.
[19] Y. Yoshida, N. Yukawa, T. Ishikawa, Determination of ductile damage parameters by notched round bar tension test using image analysis, AIP Conf. Proc. 712 (2004) 1869.
[20] J. Lemaitre, A Course on Damage Mechanics, Springer-Verlag, Berlin, 1992.